www.lpr-journal.org

Photon-Counting Compressed Spatial-Spectral Imaging for 4D Information Retrieval

Mingzhong Hu, Jingyuan Zheng, You Xiao, Hao Li, Lixing You, Yidong Huang, and Wei Zhang*

Photon-counting spectrometers based on single-photon detectors are demonstrated as highly sensitive tools for optical spectrum analysis. In this work, an imaging scheme using such devices is proposed to achieve spatial-spectral imaging for 4-D information retrieval. It combines spatial and spectral compressed sensing with depth measurement based on time-of-flight (ToF). Hence, it is named Photon-Counting Compressed Spatial-Spectral Imaging (PCCSSI). A proof-of-principle experiment is carried out with a photon-counting spectrometer based on superconducting nanowire single-photon detectors (SNSPDs) and metasurfaces. The experiment results demonstrate the principle of PCCSSI, showing its potential for high-dimensional imaging under photon-sparse scenarios, such as spectral remote sensing, spectral fluorescence imaging, etc.

1. Introduction

Optical spectrum analysis has been one of the most significant ways in modern science to study and understand the physical world.^[1,2] Spectrometers are needed to carry out optical spectrum analysis, and their sensitivity is of concern, especially for some applications where the light being measured is at the single-photon level. For instance, spectral light detection and ranging (LiDAR) at far distances and astronomical spectroscopy often deal with ultra-faint light at this level.^[3–5] Besides, Raman spectroscopy and fluorescence spectroscopy also necessitate high-sensitivity spectrometers.^[6,7] Motivated by these applications,

Beijing National Research Center for Information Science and Technology (BNRist)
Department of Electronic Engineering
Tsinghua University
Beijing 100084, China
E-mail: zwei@tsinghua.edu.cn
Y. Xiao, H. Li, L. You
State Key Laboratory of Functional Materials for Informatics
Shanghai Institute of Microsystem and Information Technology
Chinese Academy of Sciences
Shanghai 200050, China
Y. Huang, W. Zhang
Beijing Academy of Quantum Information Sciences
Beijing 100193, China

The ORCID identification number(s) for the author(s) of this article can be found under https://doi.org/10.1002/lpor.202500618

DOI: 10.1002/lpor.202500618

M. Hu, J. Zheng, Y. Huang, W. Zhang

Frontier Science Center for Quantum Information

researchers have employed singlephoton detectors to enhance the sensitivity of optical spectrum analysis.^[8,9]

Single-photon detectors, for example, photomultiplier tubes,^[10] single-photon avalanche detectors,^[11] and superconducting nanowire single-photon detectors (SNSPDs),^[12] can be used for developing high-sensitivity spectrometers. Among them, SNSPDs can achieve near-unity efficiency and ultra-low dark count and have gained significant research interest, especially in the infrared band.^[13,14] Single-photon detectors can record the single-photon detection events and implement photon-counting measurements with electrical

counters. This feature not only enables high-sensitivity optical spectrum analysis but can also obtain the temporal information of the arriving photons. The temporal information can be used for other purposes, such as time-domain spectroscopy, fluorescence lifetime imaging microscopy, LiDAR, etc.^[15–19]

Despite their excellent light detection performance, highperformance arrayed single photon detectors are still under development and not commercially available. Hence, when applied for optical spectrum analysis, they are usually combined with scanning narrowband filters such as monochromators or scanning interferometers to realize Fourier-transform spectroscopy. In early implementations with monochromators and interferometers, [20] though the system featured single-photon sensitivity and the ability to retrieve temporal information, it was bulky and lacked robustness. Scanning processes were also involved, resulting in both complex motion control and long measurement time. To address the former problem, integrated photon-counting spectrometers with no moving parts have been demonstrated for compactness and robustness.[21] Compressed sensing can be introduced to solve the latter problem. Combining integration and compressed sensing, Hartmann et al. have proposed and demonstrated an integrated reconstructive photon-counting spectrometer with no need for scanning.^[22] In this device, the out-of-plane scattering loss from the disordered scatter and the coupling loss limited its system detection efficiency. Recently, by taking a normal-incidence coupling scheme and changing the modulation structures into metasurfaces and photonic crystals, Zheng et al. and Xiao et al. mitigated the loss and increased the system detection efficiency to more than 1%.[23,24] Lately, other mechanisms for reconstructive photon-counting spectrometers, including bias current tuning

18638899, 0, Downloaded from https://onlinelibrary.wiley.com/doi/10.1002/ppr.202500618 by Tsinghua University Library, Wiley Online Library on [28/10/2025]. Sether Terms and Conditions (https://onlinelibrary.wiley.com/terms-and-conditions) on Wiley Online Library for uses of use; OA arctices are governed by the applicable Creative Commons License

Figure 1. a) The schematic diagram of PCCSSI. Active illumination is used. The reflected light from the target is compressed in spatial and spectral dimensions successively. b) Data compression and reconstruction scheme in PCCSSI. Intensity distribution over spatial 3D dimensions x, y, z, and spectral dimension λ is compressed into the n-th detector outcome under the m-th spatial compression mask patterns. (m = 1, 2, ..., M; n = 1, 2, ..., M).

and cascaded absorption, have also been investigated. [25,26] Moreover, the photon-counting ability of these spectrometers to acquire timestamps for photon arrival can enable applications for high-dimensional imaging in photon-sparse scenarios. Kong et al. obtained spatial-spectral 4D information with galvanometer scanners and their photon-counting spectrometer, which also worked as a Time-of-Flight (ToF) sensor. [25] In their work, the measurement process needs pixel-wise scanning for information in different spatial locations and bias current scanning for spectral reconstruction, which increases the number of measurements and extends the imaging time.

In this work, we propose an imaging scheme using single-photon detectors to carry out high-dimensional imaging with compressed sensing on both spectral and spatial dimensions. The scheme is named Photon-Counting Compressed Spatial-Spectral Imaging (PCCSSI). By the principles of compressed sensing, a signal can be reconstructed with good quality even when highly undersampled. In this way, PCCSSI accelerates the imaging process with fewer numbers of measurements. Besides, compressed sensing can also relax the requirement for spectral modulation. Spectral modulation does not have to be narrowband as in traditional spectrometers. It could be designed considering better structure simplicity, fabrication feasibility, and higher broadband transmission. Broadband transmission could elevate photon utilization and thus is highly important under photon-

sparse scenarios. ^[27] To demonstrate the principle of this scheme, a PCCSSI imaging system using a photon-counting spectrometer based on SNSPDs and metasurfaces is established, which is an improved device based on our previous work. ^[23] The function of high-dimensional imaging, including 3D spatial and spectral information, is demonstrated, showing the potential of PCCSSI on fast, high-dimensional imaging tasks in photon-sparse scenarios.

2. PCCSSI: The Principle

The schematic diagram of the PCCSSI system is illustrated in Figure 1a. Briefly, the scene is illuminated by a broadband pulsed laser. The spatial modulation and spectral modulation are applied on the light reflected from the scene for information compression. In the process of image reconstruction, the time-correlated single-photon counting (TCSPC) is used for depth information retrieval, and the compressed sensing algorithm is used to reconstruct spectral images at different depths.

The data compression and reconstruction scheme of the PCC-SSI system is shown in Figure 1b. PCCSSI can obtain the spatial-spectral 4D information of the targets, i.e., the intensity distribution of reflected light from the scene over the 3D-spatial and spectral dimensions: $I(x, y, z, \lambda)$. This can be discretized as a 4D data cube with a size of $D_x \times D_y \times D_z \times D_\lambda$. First, spatial compression is applied by a digital micromirror device (DMD). If M DMD



www.advancedsciencenews.com

LASER & PHOTONICS REVIEWS

www.lpr-journal.org

patterns are used as the compression mask, the spatial compression ratio is $(D_x \times D_y)$: M. Then, the light is collected and the spectral modulation is applied to it. The spectral modulation can be realized by modulating the spectral responses of the detectors, which are defined as the detection efficiencies under different wavelengths. If N detectors with different spectral responses are used, the spectral compression ratio is D_λ : N. As a result, the total compression ratio is $(D_x \times D_y \times D_\lambda)$: $(M \times N)$. Finally, the information on the z dimension, i.e., the depth information, is acquired by the ToF method. By TCSPC, the time difference τ between the photon arrival timestamps recorded by single-photon detectors and the synchronous signals from the pulsed laser is measured, and the depth information can be calculated.

For image reconstruction, the depth information can be retrieved directly from measured time differences. To reconstruct the spectral image at different depths, two methods are proposed. The first one deals with it as an optimization problem in the dimensions of x, y and λ , which is named as the joint reconstruction method. Considering that the size of the data cube is quite large, leading to high requirements on the memory size and calculation capability, this problem can be separated into two steps as two subproblems in series, thanks to the independence of spatial and spectral compression in PCCSSI. The spatial images could be reconstructed independently based on the data recorded by different detectors. Then, the spectra at different pixels in the spatial image can be retrieved based on these reconstructed spatial images. It is named the two-step reconstruction method. The performances of the two reconstruction methods are compared and analyzed in Section 4. For details of the information compression and reconstruction process, please see Note \$1 (Supporting Information).

3. Device Improvements and Characterization

We use the photon-counting spectrometer proposed in previous work for spectral compression and detection to demonstrate the PCCSSI.^[23] This device features single-photon-level spectral compressed sensing. Besides, it can record single-photon events with their arrival time. The device is improved for imaging applications, as shown in Figure 2. It has 16 detector units with different spectral responses, each comprised of an SNSPD and a metasurface, as shown in Figure 2a. In a detector unit, the SNSPD is fabricated above the metasurface and located in the spaces of the periodical micro-holes. The metasurface provides strong spectral modulation on the SNSPD. The periods and radii of the microholes varied in different units, leading to different modulations on the spectral responses of SNSPDs with low correlation that could be used for spectral compression. Figure 2b,c are scanning electron microscope (SEM) pictures of the device, showing the device structure clearly.

Three improvements are applied to the device, compared with the prototype device in the previous work.^[23] First, a fractal design is used on the SNSPDs, as shown in Figure 2a. This design reduces their polarization dependence and naturally matches the structures of metasurfaces with periodical micro-holes with C4-symmetry.^[28] The spectral responses of different SNSPDs can also be randomly modulated by the metasurfaces with different parameters. For a specific SNSPD, the input photons with different polarizations produce similar spectral responses due to this

design. It could simplify the calibration process of the device and the optical design of the imaging system. Second, the areas of the SNSPDs are redesigned to balance their detection efficiency. In this device, the SNSPDs at the edges had larger areas than those at the center, as shown in Figure 2b. The efficiency difference of the SNSPDs in different locations would be reduced by this design. Finally, a piece of multimode fiber is used to deliver photons to the device in the cryostat, which could improve the collection efficiency for photons from free space. A mode scrambler on the multimode fiber is used to stabilize the intensity profile of the input light. For details on the design and the fabrication of this device, please see Note S2 (Supporting Information).

Before the device is used as a photon-counting reconstructive spectrometer, the spectral responses of the SNSPDs are characterized. Details of the experimental setup and process of the characterization are introduced in Note \$3 (Supporting Information). The detection efficiencies under different light wavelengths of all the SNSPDs are measured and shown in Figure 2d. Detection efficiency is defined as the ratio of the counting rate of each SNSPD to the photon flux entering the multimode fiber. It shows that 12 SNSPDs have normal responses of single photon detection, which are used in the following experiments. The metasurfaces with different parameters provide different modulations on the spectral responses of these SNSPDs. The maximum efficiencies of these SNSPDs are similar, showing that the design of the detection areas on the device balanced the performances of these detectors effectively. The total detection efficiency is calculated by summing the efficiencies of all SNSPDs, which is shown in Figure 2e. The total detection efficiency of the device is \approx 7–13% in the wavelength range of 850-1200 nm, much higher than that of the prototype device in the previous work (1.1–4.44%). The dark count rates and timing jitters of the valid SNSPDs in the device are shown in Figure 2f. Using the measured spectral responses as the basis of spectral compressed sensing, the spectra of monochromatic lights are measured and reconstructed by this device. The experiment result is shown in Figure 2g. It can be seen that the spectra of monochromatic lights at different wavelengths in the range of 850-1200 nm could be reconstructed successfully. For more details on the device, including the system stability to the calibration variation and its capability to deal with complex spectra, please see Notes \$4 and \$5 (Supporting Information).

4. Imaging Results

4.1. The Experimental Setup

Using the improved device introduced in Section 3 as the device for spectral compression and detection, we set up the PCCSSI system as shown in Figure 1. A supercontinuum pulsed laser source (YSL Photonics, SC-Pro-M) is used to realize the active illumination. The pulse width of the illuminating light is ≈ 6 ps. Before illuminating the scene, the light passed through an optical bandpass filter set and is confined to a wavelength band of 890–1050 nm. A bi-concave lens (focal length = -25 mm) is used to expand the beam in illumination optics. We adopt a coaxial setup for the active illumination and the collection of reflected light, as shown in **Figure 3a**. The reflected light is imaged by a single lens (focal length = 175 mm) onto a DMD (UP-

18638899, 0, Downloaded from https://onlinelibrary.wiley.com/doi/10.1002/por.202500618 by Tsinghua University Library, Wiley Online Library on [28/10/2025]. See the Terms and Conditions

and-conditions) on Wiley Online Library for rules of use; OA articles are governed by the applicable Creative Commons License

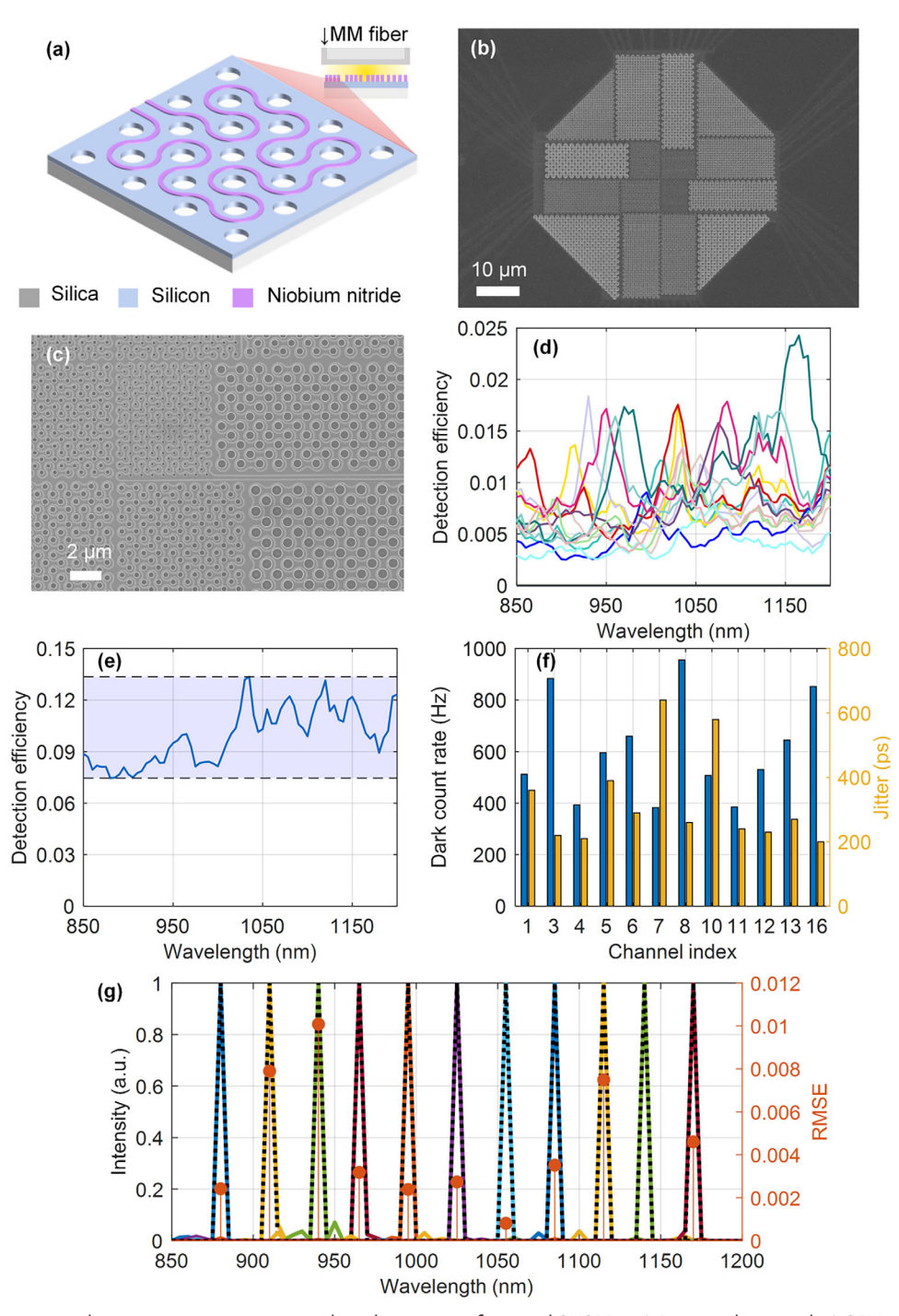


Figure 2. The reconstructive photon-counting spectrometer based on metasurfaces and SNSPDs. a) Device schematic. b,c) SEM pictures of the device (overview and local view). d) Spectral responses of different SNSPDs in the device. e) Total detection efficiency of the device. f) Dark count rates and timing jitters of valid SNSPD in the device. g) Reconstruction results (colored lines) and reference spectra (dashed lines) of single-photon-level monochromatic lights at different wavelengths. Orange dots indicate the corresponding root mean square errors (RMSE).

OLabs, HDSLM108D65NIR-DDR) for spatial compression. After the spatial compression by the DMD, the light is collected by a reflective achromatic collimator (Thorlabs, RC12APC-P01) into a multimode fiber with a core diameter of 50 microns. The fiber then sends the light to the photon-counting spectrometer for spectral compression and detection.

Four targets are set in the scene of the imaging experiment. Each includes a bandpass filter backed with a paperboard as a diffuse reflector, as shown in Figure 3a. The center wavelengths of the filters in the four targets are 905, 950, 980, and 1030 nm, respectively. Only the faint light due to the diffuse reflection of these targets is collected by tilting their orientation

18638899, 0, Downloaded from https://onlinelibrary.wiley.com/doi/10.1002/ppr.202500618 by Tsinghua University Library, Wiley Online Library on [28/10/2025]. Sether Terms and Conditions (https://onlinelibrary.wiley.com/terms-and-conditions) on Wiley Online Library for uses of use; OA arctices are governed by the applicable Creative Commons License

www.advancedsciencenews.com

www.lpr-journal.org

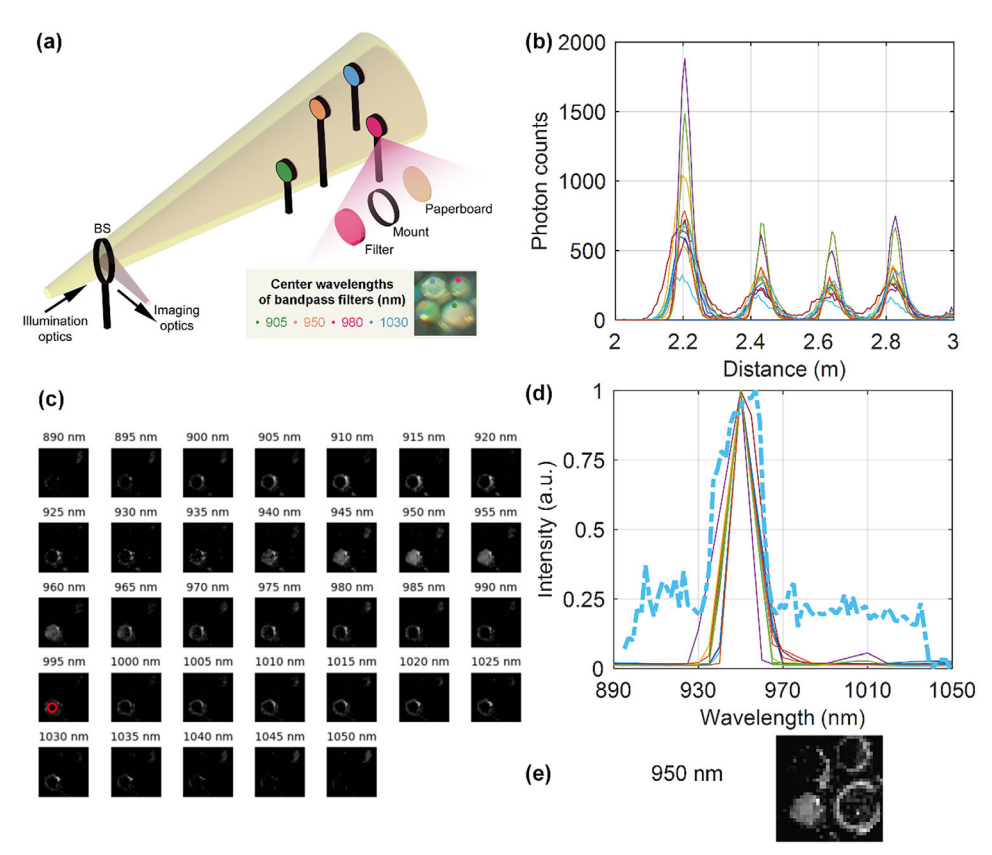


Figure 3. The scene of the PCCSSI experiment and the results of high-dimensional imaging. a) The imaging scene in the experiment includes four targets, each consisting of a bandpass optical filter and a paperboard as a diffuse reflector. The scene is illuminated through a coaxial optical system. The inset shows a photograph of the scene recorded by a visible camera from the illumination direction. The center wavelengths of the filters in the four targets are 905 nm (bottom right), 950 nm (bottom left), 980 nm (top right), and 1030 nm (top left), respectively. b) TCSPC results showing the photon count distribution at different depths of the scene. Lines of different colors represent the results of different SNSPDs of the photon-counting spectrometer. c) Reconstructed spectral images under different wavelengths at the depth of 2.83 m. d) Reconstructed spectra of the pixels (solid lines) in the red circle in (c), located on the bottom-left target, compared with the reference spectrum obtained by a commercial spectrometer (dashed line). All spectra have been normalized. e) The reconstructed image representing a section of the data cube at 950 nm. Reconstructed images in (c) and (e) are acquired under a spatial compression ratio of 1:1. A log-transform is applied to them and all the following reconstructed images for better visualization.

and avoiding the impact of specular reflection. The spectrum of the reflected light is determined by the spectrum of illumination light and the transmission spectra of the filters in the targets.

In the experiments, we use 32×32 Hadamard patterns on the DMD for spatial modulation. The exposure time for each DMD pattern is set to 1 s, and the total photon counting rate is ≈ 123 kHz under a pulse repetition frequency of 5 MHz, indicating a highly photon-sparse scenario.

4.2. The Demonstration of Spatial-Spectral Imaging

The high-dimensional imaging ability of PCCSSI is demonstrated step by step. The PCCSSI setup acquires the depth information directly from the TCSPC results, as shown in Figure 3b. There are four peaks, each of which is contributed to by the reflected photons from a specific target. A Gaussian fitting is used to find the peak position to calculate the precise depth of the target. Then, spectral images at specific depths are reconstructed using the methods introduced in Section 2.

In this subsection, the joint reconstruction method is used to reconstruct the spectral image at a specific depth with a spatial compression ratio of 1:1. Figure 3c shows the results at the depth of 2.83 m, using the single photon events of the rightmost peak shown in Figure 3b. These photons are mostly reflected by the bottom-left target shown in the inset of Figure 3a, in which the center wavelength of the optical filter is $\approx\!950$ nm. Each figure in Figure 3c shows a 2D image at a specific wavelength, as noted at the top of the figure. The brightness of these figures is normalized by the brightest pixel in them. The target can be seen clearly at a wavelength $\approx\!950$ nm. At other wavelengths, only a hollow circle can be observed, which is the metal mount of the filter and reflects photons at all wavelengths. These images do not have information about other targets since they are not at this depth.

To confirm the spectrum reconstruction under compression in PCCSSI, the spectra of all the pixels surrounded by the red circle in Figure 3c are plotted in Figure 3d. The solid lines are the reconstructed results of 12 pixels, and the blue dashed line is obtained by measuring the reflection spectrum of the specific target at a close distance with bright illumination and a commercial spectrometer (Ando AQ6317). The baseline in the reference spec-

18638899, 0, Downloaded from https://onlinelibrary.wiley.com/doi/10.1002/lpor.202500618 by Tsinghua University Library, Wiley Online Library on [28/10/2025]. See the Terms

and Conditions

and-conditions) on Wiley Online Library for rules of use; OA articles are governed by the applicable Creative Commons License

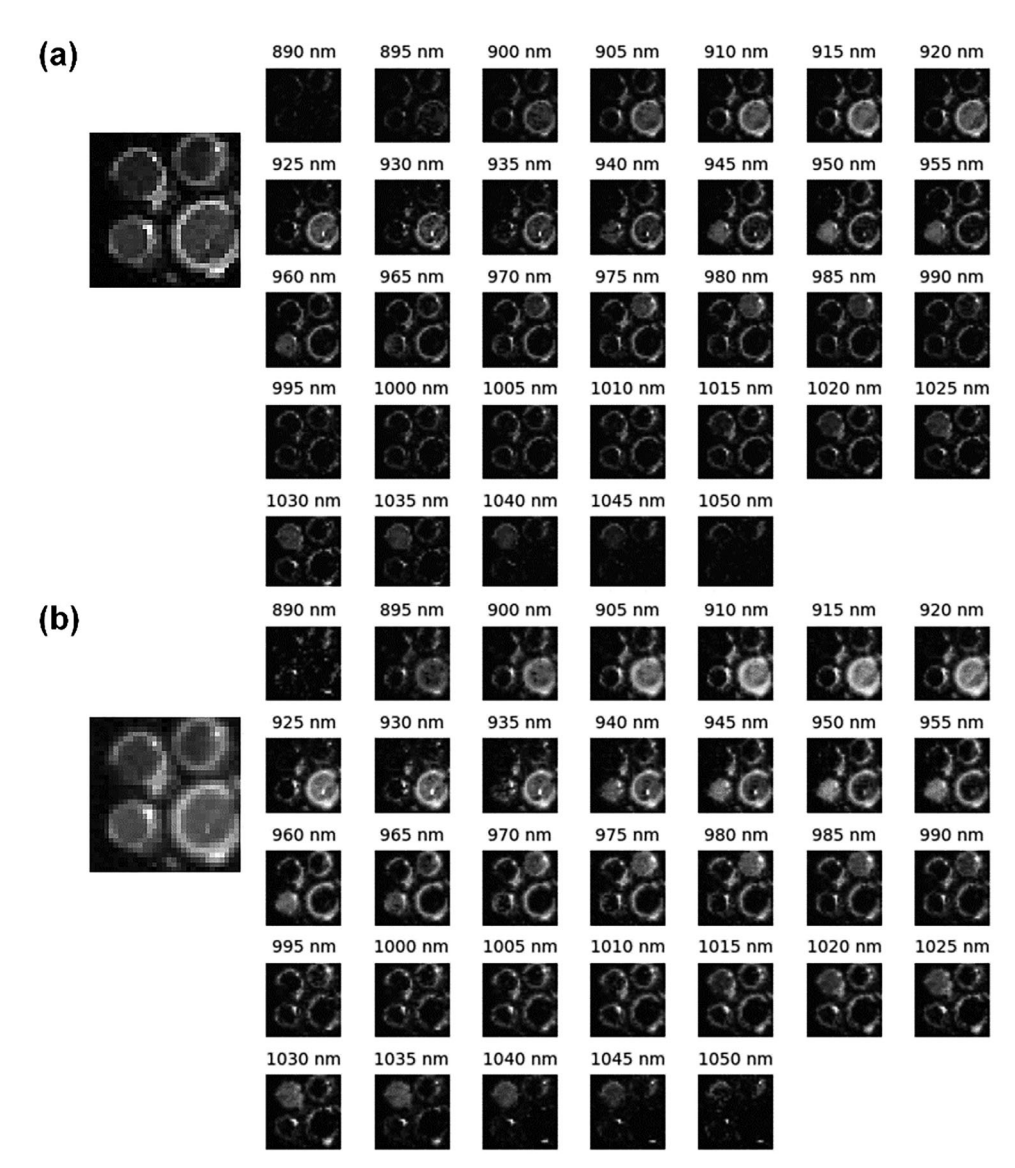


Figure 4. Reconstructed images obtained using different reconstruction methods. a) Images reconstructed by the joint reconstruction method. b) Images reconstructed by the two-step reconstruction method. The images on the right are the sections of the data cube at different wavelengths. The large images on the left side are the results with all the wavelength components. All the images are obtained under a spatial compression ratio of 1:1.

trum can be attributed to the contribution of the metal mount. It can be seen that the reconstructed results agree well with the main spectral components of the measured reference spectrum. In the reconstruction process, the outcomes of 12 valid detectors are used. On the other hand, the sample point number of the reconstructed spectra is 33 (over 890–1050 nm with a resolution of 5 nm). Hence, the spectral compression ratio is 2.75:1. Similar results can be obtained at the depths of the other three targets, using the single photon events of other peaks shown in Figure 3b.

We select the reconstructed images of 950 nm at the depths of the four targets and add them together as a section of the data cube at a specific wavelength, i.e., 950 nm. The result is shown in Figure 3e. Compared with the inset of Figure 3a, the image of 950 nm shows the full bottom-left target but only the metal filter mounts of other targets since the center wavelengths of the filters in the other three targets are not at 950 nm. These results con-

firm that the experimental system of PCCSSI can realize high-dimensional imaging with 3D spatial information and spectral information.

4.3. The Comparison of Reconstruction Methods

The performance of the joint reconstruction method and the two-step reconstruction method of PCCSSI is compared in this subsection. The results of the two methods are displayed in Figure 4a,b, respectively. The small images on the right side are the reconstructed images representing the section of the data cube at specific wavelengths, similar to Figure 3e. In the results of both methods, the inner circle part of the four targets appears in the spectral images of different wavelengths, which agrees with the center wavelengths of the optical filters in the targets. On



www.advancedsciencenews.com

LASER & PHOTONICS REVIEWS

www.lpr-journal.org

the contrary, the edges of the four targets appear in most images since the mounts of the filters reflected photons of almost all the wavelengths. These demonstrate that both methods can reconstruct the spatial-spectral information successfully.

However, the qualities of the images reconstructed by the two methods are different. The results acquired by the joint reconstruction method have a better spatial resolution than those acquired by the two-step reconstruction method. It can be seen more clearly in the two large images on the left side in Figure 4, which are results with all the wavelength components and obtained by merging all the images on the right side. The better spatial resolution benefits from considering the spatial continuity of the spectrum information in the joint reconstruction method. Intuitively, the total variation (TV) regularizer used in this work (Please see Note \$1, Supporting Information for details) provides the spectral knowledge from adjacent pixels to suppress noise in the final images. On the contrary, in the two-step reconstruction method, the spectra of different spatial pixels are reconstructed independently and highly depend on the qualities of the reconstructed images of different detectors. A strong spatial regularizer has to be employed in the first step to smooth out images and reduce the noise. As a side effect, it leads to the degradation of spatial resolution. We also compare the performance of the two reconstruction methods under different signal-to-noise levels using the experiment results under different measurement times. Details of the comparison are shown in Note \$6 (Supporting Information). It shows that the joint reconstruction method is less sensitive to the decrease of signal-to-noise than the two-step reconstruction method.

On the other hand, experiments show that the joint reconstruction method needs more calculation time for image reconstruction than the two-step reconstruction method. The algorithms of both methods are run on the same computer with an i7-12700 CPU and no GPU acceleration. The joint reconstruction method needs $\approx\!120~s$ to complete a typical reconstruction, while the two-step reconstruction method needs $\approx\!60~s$ for the same task. The two-step reconstruction method decomposes the large optimization problem in PCCSSI into multiple independent small problems that have less computational complexity. Besides, these small problems could be processed in parallel, which may make better use of the computational resources. It can be expected that the two-step reconstruction is more scalable for large scenes.

4.4. The Impact of the Spatial Compression Ratio

To show the impact of the spatial compression ratio, we reconstruct the images under different spatial compression ratios and show the results in **Figure 5**. Two metrics, the structural similarity index measure (SSIM) and peak signal-to-noise ratio (PSNR), are used to evaluate the image quality quantitatively. The reconstructed data cube obtained through the joint reconstruction under a compression ratio = 1:1 is used as the reference, and the two metrics are calculated on the reconstructed data cube, i.e., all the reconstructed 2-D spatial images at specific depths and wavelengths. The results are shown in Figure 5a,b, respectively. It can be seen that both SSIM and PSNR deteriorate when the compression ratio increases. To show the deterioration visually, we add these 2-D spatial images obtained under a specific spatial

compression ratio together, showing the results under compression ratios of 2.13:1, 9.06:1, and 25:1 in Figure 5c–e. Their SSIM and PSNR are marked by the solid dots with different colors in Figure 5a,b. An SSIM of 0.9 and a PSNR of 30 dB are commonly used as thresholds for acceptable image quality. It can be seen that the acceptable spatial compression ratio is \approx 10:1 for the experimental system in this work, which corresponds to an imaging time of \approx 3 min.

As a glimpse of the quality of spectrum reconstruction, the reconstructed spectra of pixels in the bottom-left targets are shown in Figure 5f (the pixels are in the region marked by the red circle in Figure 3c). Reconstructed spectra of different pixels under the same compression ratio are labelled with the same color. It can be seen that the quality of spectrum reconstruction does not change significantly under different spatial compression ratios, since the spatial compression and spectral compression are independent in this system.

5. Discussion

To show its advantages, PCCSSI is compared with previous works of single-photon imaging and spectroscopy systems, as shown in **Table 1**. The normalized measurement time is used to compare the imaging systems with different image sizes, spectral ranges, and photon counting rates. It is defined by dividing the total measurement time by the pixel number of the spectral–spatial data cube when the photon counting rate is normalized to 1 MHz. The detection efficiencies of different systems are also compared. Note that the reported detection efficiencies refer to the detection system only and exclude losses from the imaging or collecting optics, since they are designed on a case-by-case basis according to their imaging or spectroscopy tasks.

The first four works in Table 1 are recent representative works of single-photon 2D imaging and 3D imaging.[18,29-31] Compressed sensing is applied in the single-photon 2D transmission imaging in the mid-IR band to overcome the difficulties of highsensitivity arrayed detectors in this band. [29] In single-photon 3D reflection imaging, image reconstruction can be achieved under ultra-low numbers of detected photons through advanced algorithms based on strong prior information (e.g., a single depth peak in the histogram and spatial correlations), leading to very short normalized measurement times. [18,30] Utilizing prior information, a relatively short normalized measurement time is also achieved even under an extremely low signal-to-noise ratio of 5×10^{-4} .[31] The next two works are about single-photon reconstructive spectrometers. They benefit from compressed sensing to reduce measurement times.^[23,32] However, their normalized measurement times are much higher than those of the works of single-photon 2D imaging and 3D imaging. The last two works, including this work, are about single-photon spatialspectral imaging. Comparing with the previous work, [25] PCC-SSI in this work uses compressed sensing on both the spectral dimension and the spatial dimension, significantly reducing the number of measurements with a high compression ratio. In addition, spatial correlations are exploited during reconstruction. Hence, the normalized measurement time in this work is much shorter than that of Ref. [25] and works about single-photon reconstructive spectrometers, setting a new benchmark of photoncounting spatial-spectral 4D imaging. Moreover, it can be seen

18638899, 0, Downloaded from https://onlinelibrary.wiley.com/doi/10.1002/lpor/202500618 by Tsinghua University Library, Wiley Online Library on [28/10/2025]. See the Terms and Conditions (https://onlinelibrary.wiley.com/terms

and-conditions) on Wiley Online Library for rules of use; OA articles are governed by the applicable Creative Commons License

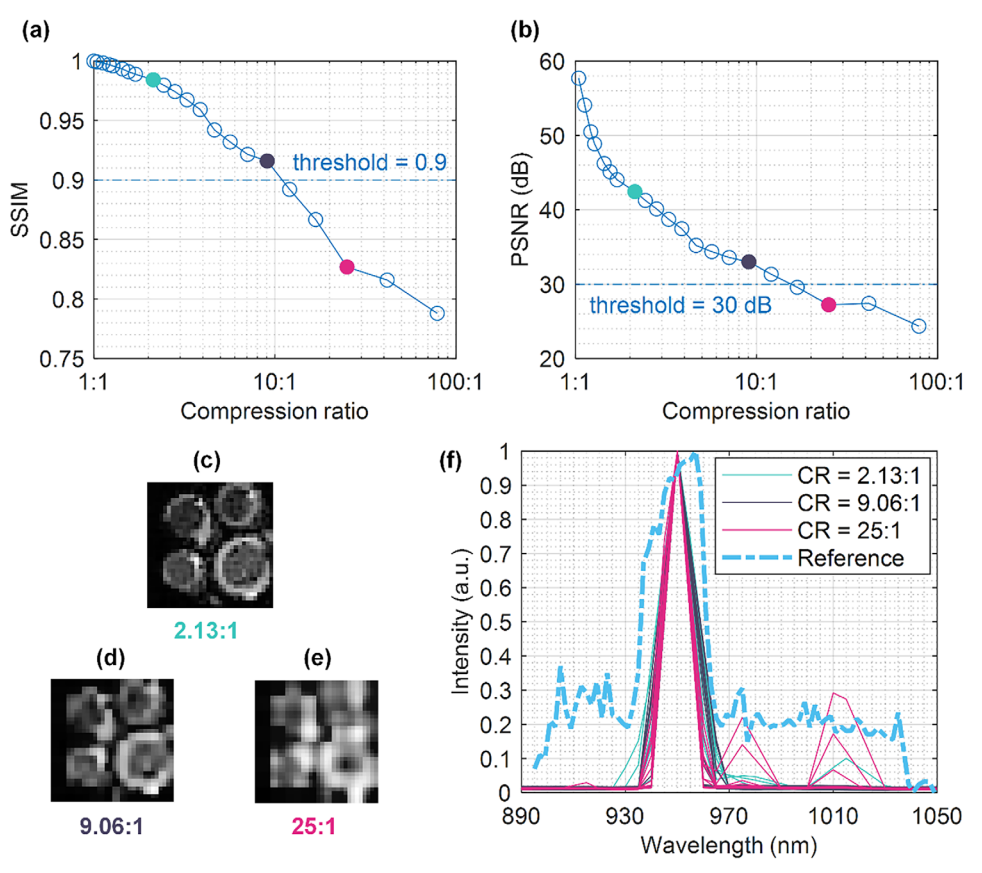


Figure 5. The impacts of the spatial compression ratio. a) Structural similarity index measure (SSIM) and b) peak signal-to-noise ratio (PSNR) under different spatial compression ratios (plotted in log scale). c—e) Visual results at different compression ratios, obtained by adding the 2D spatial images obtained under specific spatial compression ratios together. The corresponding SSIMs and PSNRs are marked in (a) and (b) by solid dots with different colours. f) Reconstructed spectra under different spatial compression ratios (CR) of the pixels in the red circle in Figure 3c, which are on the bottom-left target. The reconstructed spectra of different pixels (solid lines) are grouped by the spatial CR and labelled by different colors. The reference spectrum (dashed line) was obtained by a commercial spectrometer. All spectra have been normalized.

Table 1. Comparison of recent works on single-photon imaging and spectroscopy.

References	Operation Wavelength Range [nm]	Spectral acquisition/Resolution [nm]	Depth acquisition	Imaging method	CR ^{a)}	Normalized measurement time [ms] ^{b)}	Detection Efficiency ^{c)}
Wang et al.[29]	3070	×	×	DMD(CSd))	4:1	9.20	0.504%
Li et al. ^[18]	1550	×	ToF	Scan	N/A	4.40×10^{-4}	19.3%
Liu et al.[30]	532	×	ToF	DMD	N/A	1.45×10^{-4}	N/A
Fang et al.[31]	3070	×	Upconversion Gating	Array	N/A	0.375	0.256%
Zheng et al.[23]	1500–1600	Metasurface (CS ^{d)})/2	×	×	5:1	17.2	1.4%-3.2%
Sun et al. ^[32]	3100–3900	Grating DMD(CS ^{d)})/0.6	×	×	2:1	46.6	0.03%
Kong et al.[25]	1000-1700	Bias scan/100	ToF	Scan	1:1	~1000	$\sim 10^{-6}$
This work	850-1200	Metasurface (CSd))/5	ToF	DMD (CSd))	25:1	0.823	7%–13%

a) Compression ratio. b) Total measurement time divided by the number of data points in the spectral–spatial data cube, normalized to a counting rate of 1 MHz. c) Ratio of input photon flux at the entrance of the detection system (after the imaging object) to the photon counting rate. d) CS: Compressed sensing. The details for the data shown in this table are introduced in Note S7 (Supporting Information).

LASER & PHOTONICS REVIEWS

that the photon-counting spectrometer used in this work features a high detection efficiency compared with other works in Table 1. It is also helpful to further reduce the imaging time.

However, the typical imaging time is several minutes in the proof-of-principle experiment of this work. There are several ways to further reduce the imaging time. First, the compression ratio has room for improvement. Since the spectral compression is realized by the arrayed detectors with different spectral responses, the number of measurements in the imaging process is determined by the spatial compression ratio, which is \approx 10:1 in this experiment, to achieve an acceptable image quality. A spatial compression ratio of more than 10:1 is readily accessible in stateof-the-art single-pixel imaging systems by employing neural network algorithms. [33,34] Such algorithms could be used in PCCSSI. Second, in the experiment setup in this work, the imaging optics system with an aperture of ≈ 0.05 is too simple to support a high photon collection efficiency. The coupling efficiency of photons to the optical fiber can also be further increased. The performance of the experimental system could be improved by optimizing its optical design. Finally, the efficiencies and maximum counting rates of SNSPDs in the photon-counting spectrometer also have significant potential for improvement through optimization of the device design and fabrication process. These improvements are expected to significantly reduce the imaging time and enable real-time measurement based on PCCSSI.

For the potential application of PCCSSI, the ability to obtain depth information by ToF makes it suitable for remote sensing. Compared with other methods, for example, stereo vision, [35] light field camera, [36] and amplitude-modulated continuous wave ToF, [19] the depth resolution in PCCSSI is determined by the timing jitter of the single-photon detectors and does not depend on the distance or signal intensity. [37] Hence, PCCSSI could be used as a spectral LiDAR with high depth resolution.

Another feature of PCCSSI is its high sensitivity thanks to its photon-counting measurement. This feature is highly valuable under photon-sparse scenarios, such as high-dimensional imaging in Raman and fluorescence measurement, especially when their pump lights are weak. The generated photons can be better utilized by PCCSSI compared with traditional spectral imaging techniques based on multiple narrow-band filters.

It is worth noting that the single photon detections in PCCSSI could record the arrival time of the detected photons. This feature can also be used to measure the fluorescence lifetime. Hence, PCCSSI also has the potential to be used in spectrally resolved fluorescence lifetime imaging microscopy in illumination-limited scenarios.

6. Conclusion

In this work, we propose an imaging scheme based on photoncounting spectrometers. It is named PCCSSI and performs highdimensional imaging with compressed sensing on both spectral and spatial dimensions. In this scheme, the spatial compression is achieved by spatial light modulators, similar to single-pixel imaging. The spectral compression is realized by reconstructive photon-counting spectrometers. The depth information is obtained by ToF with broadband pulsed illumination and photoncounting measurement. A proof-of-principle experiment is carried out using an improved reconstructive photon-counting spectrometer based on SNSPDs and metasurfaces. The experimental results show that PCCSSI can reconstruct 3D spatial information and 1D spectral information under photon-sparse scenarios. Its performance could be further improved by optimizing the illumination/imaging optics, the photon-counting spectrometer, and the reconstruction algorithms. As a promising way to achieve spatial-spectral 4D imaging with high sensitivity, PCCSSI has great potential for imaging applications under photon-sparse scenarios, such as spectral remote sensing, Raman spectroscopic imaging, and fluorescence imaging (especially SFLIM).

Supporting Information

Supporting Information is available from the Wiley Online Library or from the author.

Acknowledgements

M.H. and J.Z. contributed equally to this work. This work was supported by the National Key R&D Program of China (2023YFB2806700), National Natural Science Foundation of China (92365210), Natural Science Foundation of Beijing (Z180012), and Tsinghua Initiative Scientific Research Program.

Conflict of Interest

The authors declare no conflict of interest.

Data Availability Statement

The data that support the findings of this study are available from the corresponding author upon reasonable request.

Keywords

compressed sensing, high-dimensional imaging, photon-counting spectrometers, single-photon detection, superconducting nanowire single-photon detectors

Received: March 19, 2025 Revised: August 4, 2025 Published online: 1863899, Downloaded from https://olnielibrary.wiley.com/doi/10.1002/por.202500618 by Tsinghua University Library. Wiley Online Library on [28/10/2025]. Set he Terms and Conditions (https://onlinelibrary.wiley.com/terms-and-conditions) on Wiley Online Library for rules of use; OA articles are governed by the applicable Creative Commons Licensea

- [1] Z. Yang, T. Albrow-Owen, W. Cai, T. Hasan, Science 2021, 371, 722.
- [2] S. N. Spectrometers, Nat. Photonics 2009, 3, 601.
- [3] A. M. Wallace, A. McCarthy, C. J. Nichol, Ximing Ren, S. Morak, D. Martinez-Ramirez, I. H. Woodhouse, G. S. Buller, *IEEE Trans. Geosci. Remote Sens.* 2014, 52, 4942.
- [4] N. Blind, E. Le coarer, P. Kern, S. Gousset, Opt. Express 2017, 25, 27341.
- [5] A. J. Metcalf, T. Anderson, C. F. Bender, S. Blakeslee, W. Brand, D. R. Carlson, W. D. Cochran, S. A. Diddams, M. Endl, C. Fredrick, S. Halverson, D. D. Hickstein, F. Hearty, J. Jennings, S. Kanodia, K. F. Kaplan, E. Levi, E. Lubar, S. Mahadevan, A. Monson, J. P. Ninan, C. Nitroy, S. Osterman, S. B. Papp, F. Quinlan, L. Ramsey, P. Robertson, A. Roy, C. Schwab, S. Sigurdsson, et al., Optica 2019, 6, 233.



18638899, 0, Downloaded from https://onlinelibrary.wiley.com/doi/10.1002/lpor.202500618 by Tsinghua University Library, Wiley Online Library on [28/10/2025]. See the Terms

and Conditions

(https://onlinelibrary.wiley.com/terms

on Wiley Online Library for rules

of use; OA articles

are governed by the applicable Creative Commons I

- [6] A. J. Bares, M. A. Mejooli, M. A. Pender, S. A. Leddon, S. Tilley, K. Lin, J. Dong, M. Kim, D. J. Fowell, N. Nishimura, C. B. Schaffer, *Optica* 2020, 7, 1587.
- [7] J. Chan, S. Fore, S. Wachsmann-Hogiu, T. Huser, Laser Photon. Rev. 2008, 2, 325.
- [8] L. Chen, J. A. Lau, D. Schwarzer, J. Meyer, V. B. Verma, A. M. Wodtke, Science 2019, 363, 158.
- [9] O. Kahl, S. Ferrari, V. Kovalyuk, A. Vetter, G. Lewes-Malandrakis, C. Nebel, A. Korneev, G. Goltsman, W. Pernice, Optica 2017, 4, 557.
- [10] Hamamatsu Learning Center, M. Abramowitz, M. W. Davidson, https://hamamatsu.magnet.fsu.edu/articles/photomultipliers.html, (accessed: March 2025).
- [11] F. Zappa, S. Tisa, A. Tosi, S. Cova, Sens. Actuators, A 2007, 140, 103.
- [12] M. Hu, J. Zheng, K. Cui, W. Zhang, Y. Huang, Electromagnetic Science 2024. 2. 1.
- [13] G. G. Taylor, A. B. Walter, B. Korzh, B. Bumble, S. R. Patel, J. P. Allmaras, A. D. Beyer, R. O'Brient, M. D. Shaw, E. E. Wollman, *Optica* 2023, 10, 1672.
- [14] J. A. Lau, V. B. Verma, D. Schwarzer, A. M. Wodtke, Chem. Soc. Rev. 2023, 52, 921.
- [15] B. Sun, K. Huang, H. Ma, J. Fang, T. Zheng, Y. Chu, H. Guo, Y. Liang, E. Wu, M. Yan, H. Zeng, *Laser Photon. Rev.* 2024, 18, 2301272.
- [16] A. Ghezzi, A. J. M. Lenz, F. Soldevila, E. Tajahuerce, V. Vurro, A. Bassi, G. Valentini, A. Farina, C. D'Andrea, APL Photonics 2023, 8, 046110.
- [17] M. Caccia, L. Nardo, R. Santoro, D. Schaffhauser, Nucl. Instrum. Methods Phys. Res. A 2019, 926, 101.
- [18] Z.-P. Li, J.-T. Ye, X. Huang, P.-Y. Jiang, Y. Cao, Y. Hong, C. Yu, J. Zhang, Q. Zhang, C.-Z. Peng, F. Xu, J.-W. Pan, Optica 2021, 8, 344.
- [19] N. Li, C. P. Ho, J. Xue, L. W. Lim, G. Chen, Y. H. Fu, L. Yao, T. Lee, Laser Photonics Rev. 2022, 16, 2100511.
- [20] L.i Chen, D. Schwarzer, J. A. Lau, V. B. Verma, M. J. Stevens, F. Marsili, R. P. Mirin, S. W. Nam, A. M. Wodtke, Opt. Express 2018, 26, 14859.

- [21] R. Cheng, C. L. Zou, X. Guo, S. Wang, X. Han, H. X. Tang, *Nat. Commun.* 2019, 10, 4104.
- [22] W. Hartmann, P. Varytis, H. Gehring, N. Walter, F. Beutel, K. Busch, W. Pernice, Nano Lett. 2020, 20, 2625.
- [23] J. Zheng, Y. Xiao, M. Hu, Y. Zhao, H. Li, L. You, X. Feng, F. Liu, K. Cui, Y. Huang, W. Zhang, *Photonics Res.* **2023**, *11*, 234.
- [24] Y. Xiao, S. Wei, J. Xu, R. Ma, X. Liu, X. Zhang, T. H. Tao, H. Li, Z. Wang, L. You, Z. Wang, ACS Photonics 2022, 9, 3450.
- [25] L. Kong, Q. Zhao, H. Wang, J. Guo, H. Lu, H. Hao, S. Guo, X. Tu, L. Zhang, X. Jia, L. Kang, X. Wu, J. Chen, P. Wu, *Nano Lett.* 2021, 21, 9625.
- [26] J. Zheng, Y. Xiao, M. Hu, H. Li, L. You, X. Feng, X. Feng, F. Liu, K. Cui, Y. Huang, W. Zhang, Adv. Dev. Instrum. 2023, 4, 0021.
- [27] L. Bian, J. Suo, G. Situ, Z. Li, J. Fan, F. Chen, Q. Dai, Sci. Rep. 2016, 6, 24752.
- [28] X. Chi, K. Zou, C. Gu, J. Zichi, Y. Cheng, N. Hu, X. Lan, S. Chen, Z. Lin, V. Zwiller, X. Hu, Opt. Lett. 2018, 43, 5017.
- [29] Y. Wang, K. Huang, J. Fang, M. Yan, E. Wu, H. Zeng, Nat. Commun. 2023. 14, 1073.
- [30] X. Liu, J. Shi, L. Sun, Y. Li, J. Fan, G. Zeng, Opt. Express 2020, 28, 8132.
- [31] J. Fang, K. Huang, E. Wu, M. Yan, H. Zeng, Light: Sci. Appl. 2023, 12, 144
- [32] B. Sun, K. Huang, H. Ma, J. Fang, T. Zheng, R. Qin, Y. Chu, H. Guo, Y. Liang, H. Zheng, Laser Photon. Rev. 2024, 19, 2401099.
- [33] G. Situ, F. Wang, C. Wang, S. Han, D. Chenjin, *Photonics Res.* 2021, 10. 104.
- [34] X. Song, X. Liu, Z. Luo, J. Dong, W. Zhong, G. Wang, B. He, Z. Li, Q. Liu, Opt. Express 2024, 32, 3138.
- [35] J. J. Aguilar, F. Torres, M. A. Lope, Measurement 1996, 18, 193.
- [36] T. E. Bishop, P. Favaro, IEEE Trans. Pattern Anal. Mach. Intell. 2012, 34 972
- [37] M. J. Sun, J. M. Zhang, Sensors 2019, 19, 732.